Optogenetically controlled cargo shows full length human myosin VI integrates activation signals *in vivo* and *in vitro*

Alexander R. French[1], Tobin R. Sosnick[1,2*], & Ronald S. Rock[1,2*],

[1]Department of Biochemistry and Molecular Biology

[2]Institute for Biophysical Dynamics

The University of Chicago

[*]To whom correspondence should be addressed: trsosnic@uchicago.edu, rrock@uchicago.edu

Abstract

Myosins are force-producing motor proteins that play countless critical roles in the cell, each requiring it to be activated at a specific location and time. To control myosin VI with this specificity, we created a novel optogenetic tool for activating myosin VI by fusing the light-sensitive *Avena sativa* phototropin1 LOV2 domain to a peptide from Dab2 (LOVDab), a myosin VI cargo protein. Our approach harnesses the native activation mechanism of myosin VI, allowing direct inferences on myosin VI function. LOVDab robustly recruits human full length myosin VI to various organelles *in vivo* and hinders peroxisome motion in a light-controllable manner. LOVDab activates myosin VI in an *in vitro* gliding filament assay, where lipid cargo sensitizes myosin VI to activation by LOVDab. Our results support a new model of myosin VI regulation whereby myosin VI integrates Ca^{2+}, lipid, and protein cargo signals in the cell to deploy in a site-specific manner.

Introduction

Motor proteins play countless roles in biology, each requiring the motor to be recruited and activated at a particular time and place inside the cell. To dissect these multiple roles, we must develop tools that allow us to control the recruitment and activation process. One promising technique for achieving this goal is through optogenetics (1). Optogenetics involves the engineering and application of optically-controlled, genetically encoded proteins, and is transforming the fields of neuro- and cell biology (2, 3). A major benefit of optogenetics is that proteins are activated using light, which allows for high temporal and spatial control over their protein of interest.

Myosin VI is a motor protein whose study could particularly benefit from optogenetic control. It is the only myosin known to walk toward the pointed end of actin filaments (5, 6). This property enables it to perform a diverse array of cellular functions including cell division, endosome trafficking, autophagy, and Golgi and plasma membrane anchoring (7-10). Myosin VI is also auto-inhibited, a property that is commonly found in other myosins (11). When myosin VI binds to cargo through specialized adaptor

25 proteins, this auto-inhibition is relieved through a poorly understood mechanism likely involving the
26 disruption of an interaction between its cargo binding domain (CBD) and the myosin head (12, 13).
27 Dissociation of the CBD from the head both frees the head to bind tightly to actin and exposes
28 dimerization sites throughout the tail domain of myosin VI, allowing it to become a processive dimer (4,
29 16, 17). In some cases, myosin VI could conceivably function as a monomer, for example when fulfilling
30 its role as a membrane tether during spermatid individualization (18). If this is the case, more work is
31 needed to elucidate the cellular signals that determine its oligomeric state at each site of action.

32 Myosin VI has two classes of cargo proteins that bind to distinct, conserved motifs on the myosin VI
33 C-terminus (22). Disabled2, or Dab2, belongs to the class of cargo proteins that bind to a conserved
34 WWY site on myosin (23). Optineurin (OPTN) is a member of the second class that binds to a conserved
35 RRL motif (19). Binding to members of either of these classes of cargo protein is thought to relieve the
36 auto-inhibition through the mechanism described above. Recently, however, myosin VI's activation
37 mechanism has been found to be more elaborate, with evidence now showing that myosin VI binds
38 specifically to the signaling lipid PI(4,5)P_2 as well as being activated using Ca^{2+} (23, 24). The outstanding
39 questions on its activation mechanism, together with its many roles throughout the cell, make myosin VI
40 an ideal target for optogenetic study.

41 One highly successful optogenetic strategy is to use or modify naturally-occurring light sensitive
42 proteins that directly alter a cellular property of interest, such as using channel rhodopsin to manipulate
43 membrane ion gradients (1). Another method is to fuse a target protein to a naturally light-sensitive
44 protein that undergoes a conformational change in response to light. The new fusion protein is designed
45 such that it sterically blocks the target protein's binding to its partner in the dark state, but releases it in
46 the lit state.

47 This latter engineering strategy has been employed using a variety of light-sensitive proteins,
48 including phytochromes (25, 26), cryptochromes (27), photoactive yellow protein (PYP) (28), and the

49 Light, Oxygen, Voltage sensing domain 2, or LOV2, from *Avena sativa* phototropin1 (29-31). Each system
50 has its own benefits (1), but we proceeded with the LOV2 domain due to its ability to cage a peptide in
51 the dark, and expose it to binding effectors in the light. The ~150 AA domain binds a flavin
52 mononucleotide (FMN) and undergoes a conformational change involving the unfolding of its N- and C-
53 terminal helices upon absorbing blue light ($\lambda_{max} \approx$ 447nm) (32). Specifically, absorption leads to the
54 formation of a covalent bond between the FMN's C4a atom and the sulfur atom of the catalytic cysteine
55 residue C450 (33, 34). This event triggers the unfolding of both the A'α helix at its N-terminus and the
56 larger Jα helix at its C-terminus (35, 36). When the light stimulus is removed, the protein-FMN bond
57 spontaneously hydrolyses in the dark on the seconds to minutes time scale followed by rapid refolding
58 of the A'α and Jα helices, thus completing the photocycle (34-36). The degree of this conformational
59 change and the rate at which the helices refold in the dark can be independently altered by mutation
60 (36, 37) which can be useful for tuning a photoswitch (29, 30).

61 Previously, we engineered the LOV2 domain to control DNA binding (38) as well as to sterically
62 block, or "cage," a small PDZ domain-binding peptide that was fused to the C-terminal Jα helix (30). In
63 the latter system, the light-induced unfolding of the Jα helix uncages the peptide and recruits PDZ
64 domain-tethered proteins *in vivo*. This strategy has been utilized by others for the control of a variety of
65 protein-protein interactions (39) including most recently epigenetic modifications (40).

66 Here we apply a similar uncaging strategy to engineer a LOV2 fusion protein that can recruit myosin
67 VI in a light controllable manner. A short peptide region from the myosin VI cargo protein Dab2
68 (Dab2^{pep}) has been crystallized in complex with the cargo binding domain (CBD) of myosin VI, and shown
69 to recruit the myosin VI tail *in vivo* (17). Phichith *et al*. independently were able to activate full-length
70 porcine myosin VI *in vitro* using high concentrations of a Dab2 truncation that included Dab2^{pep} (4).
71 Additionally, ITC experiments suggest that the N-terminal α-helix of Dab2^{pep} contains most of its binding
72 affinity for myosin VI, making Dab2^{pep} a suitable target for caging by the LOV2 domain.

73 Here we engineer and apply an optogenetic activator for full-length human myosin VI using a LOV2-
74 Dab2^{pep} fusion protein termed "LOVDab". LOVDab robustly recruits myosin VI to a variety of cellular
75 organelles in a light-dependent manner. Recruitment of myosin VI to peroxisomes slows their velocity,
76 demonstrating myosin VI activation upon recruitment *in vivo* that is consistent with an anchoring role
77 for myosin VI. We also purify full-length human myosin VI and demonstrate its photoactivation *in vitro*
78 using a modified gliding filament assay. Lastly, we interrogate the interplay of lipid and cargo proteins in
79 activating myosin VI, and show that the presence of PI(4,5)P_2 enhances myosin VI's affinity for Dab2^{pep}.

80 Results

81 LOVDab design and optimization

82 To obtain light-controlled activation of myosin VI, we fused the portion of its cargo protein Dab2 (res.
83 674-711, Dab2^{pep}) that binds to the myosin VI cargo binding domain (CBD) to the C-terminus of the LOV2
84 Jα helix. In the crystal structure of the CBD-Dab2^{pep} complex, two CBDs and two Dab2^{pep} molecules form
85 a tetrameric structure (**Figure 1A**). Each Dab2^{pep} in the tetramer contains two helical regions that
86 contact the CBDs. The two helices bind to opposite CBDs so that each Dab2^{pep} binds across both CBDs in
87 the tetramer. The modest interface between the two CBDs in the tetramer suggests that two Dab2^{pep}s
88 promote myosin VI dimerization by tethering two myosin VI molecules in close proximity to each other,
89 disrupting the interaction of the CBD to the myosin VI head domain and promoting myosin VI
90 dimerization at various sites along its tail domain (4, 16, 17). Whether Dab2^{pep} directly competes with
91 the interaction between the CBD and the myosin VI head is unknown. ITC measurements indicate that
92 the majority of the binding affinity for the CBD lies in the N-terminal helix of Dab2^{pep} (17). Taken
93 together, these observations suggest that light-induced uncaging of the N-terminal region of two
94 Dab2^{pep} peptides may be sufficient to control myosin VI dimerization. Furthermore, the 2:2
95 stoichiometry of the CBD_2:Dab2$^{pep}{}_2$ tetramer results in a binding reaction dependent on the square of
96 the concentration of Dab2^{pep}, which should amplify the switching capability of our design.

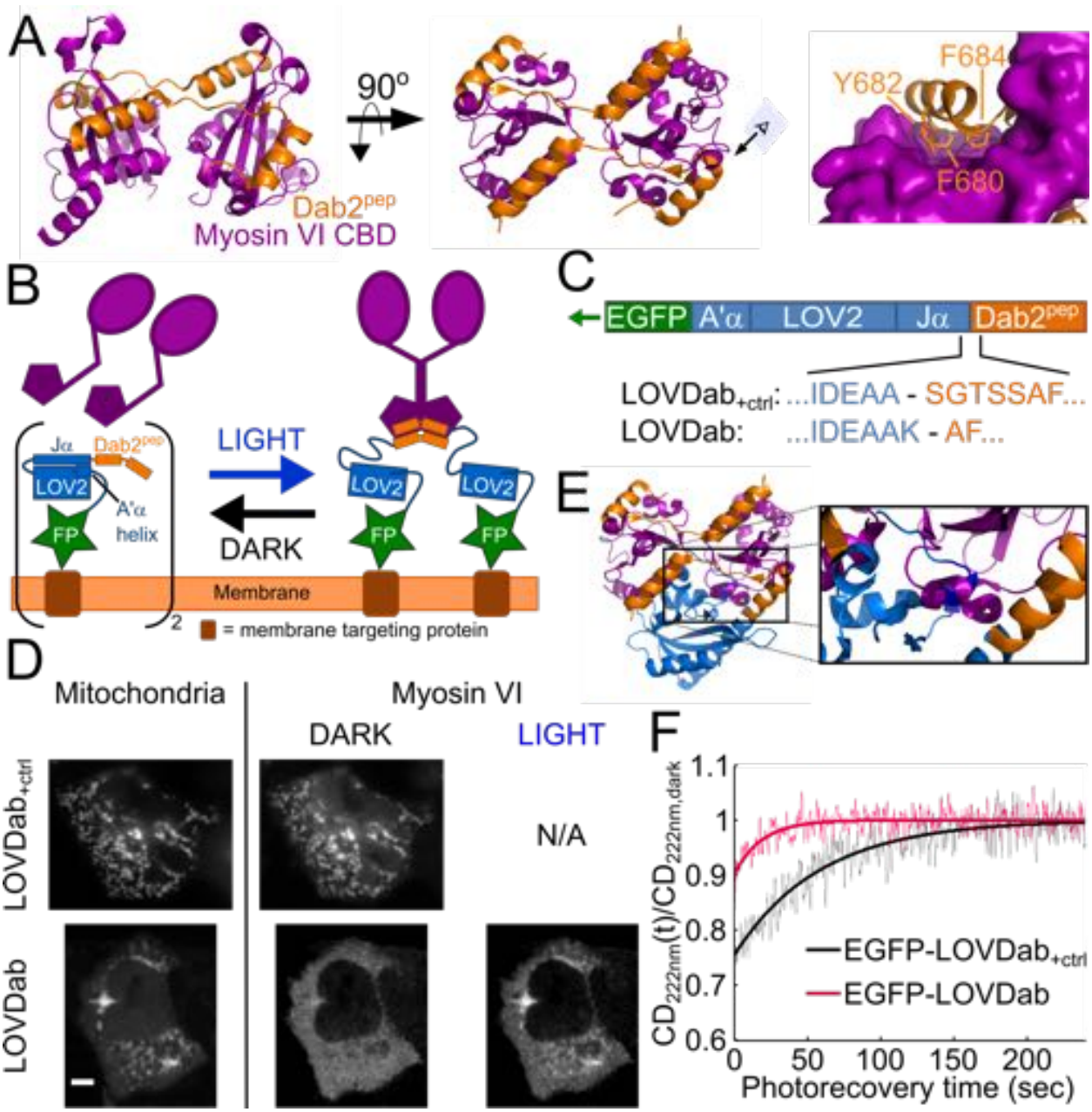

Figure 1: Design of LOVDab. (**A**) *Left and center*: The myosin VI CBD co-crystalized with Dab2^{pep} in two orientations illustrating how two Dab2^{pep} molecules straddle the CBDs. *Right*: View of N-terminal Dab2^{pep}:CBD binding interface with aromatic residues shown in sticks. (**B**) Diagram of desired function of LOVDab. In the dark, Dab2^{pep} is prevented from binding myosin VI. When excited by blue light, the A'α and Jα helices of LOV2 unfold, releasing Dab2^{pep} to recruit myosin VI to the membrane. An N-terminal tag targets LOVDab to a specific organelle in the cell. (**C**) Domain architecture of EGFP-LOVDab with the sequences of LOVDab$_{+ctrl}$ and LOVDab at the fusion site. (**D**) Recruitment assay from (**B**) performed using the constructs in (**C**). LOVDab$_{+ctrl}$ does not cage Dab2^{pep} in the dark whereas LOVDab only recruits myosin VI to the mitochondria in the lit state. Scale bar: 5 μm. (**E**) Alignment of LOV2 with Dab2^{pep}:CBD crystal structure (with zoom to boxed region on right) suggests LOVDab obstructs myosin VI binding to Dab2^{pep} in the dark. Dark blue: A'α helix. (**F**) Time course of dark state photorecovery of constructs in (**B**) measured by circular dichroism (CD) at 222nm normalized to their respective values in the dark state. At time = 0 sec the LOV2 domains are fully excited and allowed to recover in the dark.

97

98 Myosin VI cargo proteins tether myosin VI to membrane-bound organelles *in vivo.* Accordingly, we
99 tested our designs using an assay that would recruit myosin VI to various membranes in the cell (**Figure**
100 **1B**). Mitochondria were an ideal first choice for such an assay since proteins can be targeted to the
101 mitochondrial membrane by fusing the Tom70 transmembrane helix ($Tom70^{helix}$) to their N-termini (30).
102 Additionally, myosin VI is not known to act on mitochondria, and overexpression of myosin VI in the cell
103 should therefore not lead to increased background binding of myosin VI to this organelle. We thus
104 cotransfected HeLa cells with $Tom70^{helix}$-Fluorescent Protein (FP)-LOVDab and -$LOVDab_{+ctrl}$ fusion
105 proteins and full-length human myosin VI tagged with a complimentary FP on its N-terminus. Because
106 the absorption λ_{max} of EGFP is similar to that of LOV2, we alternate which of two FPs, mCherry or EGFP,
107 is on myosin VI and which is on LOVDab. The protein we intend to watch in both the light and the dark
108 states of LOV2 is fused to mCherry in order to avoid simultaneous excitation of LOV2.

109 We first tested whether $Dab2^{pep}$ is sufficient to recruit full-length myosin VI using an uncaged,
110 constitutively open fusion of $Dab2^{pep}$ to the C-terminus of the LOV2 Jα helix (**Figure 1C**). Residues 674-
111 679 of $Dab2^{pep}$ are mostly glycine and serine, suggesting that these residues could serve as a flexible
112 linker between the LOV2 domain and the remaining residues in $Dab2^{pep}$. This flexibility should prevent
113 caging of the myosin VI binding site on $Dab2^{pep}$ even when the Jα helix is folded in the dark. As expected,
114 LOV2 fused to the full $Dab2^{pep}$ sequence recruits myosin VI to mitochondria in the dark (**Figure 1D**).
115 Myosin VI is seen on puncta that correspond to the mitochondria visualized in the $LOVDab_{+ctrl}$ channel.
116 We refer to this construct as $LOVDab_{+ctrl}$ (**Figure 1C**), since it is always myosin VI binding-competent.

117 Having established that $Dab2^{pep}$ is sufficient for myosin VI recruitment, we next sought to re-
118 engineer $LOVDab_{+ctrl}$ to have light-dependent binding. Our strategy focuses on caging the aromatic
119 residues F680, Y683, and F684 on the $Dab2^{pep}$'s N-terminal helix that are buried upon CBD binding
120 (**Figure 1A**, right panel). These three residues must be close enough to the Jα helix that they are
121 sterically prevented from binding the CBD when the Jα helix is folded in the LOV2 dark state. This

122 criterion is accomplished by reducing the number of intervening residues while maintaining a
123 continuous helix encompassing the Jα helix and the N-terminal helix of Dab2^{pep}. An additional variable is
124 helical registry which controls the relative orientation of the Jα and the Dab2^{pep} helices, and therefore
125 the angle of the CBD-binding residues in Dab2^{pep} with respect to the LOV2 domain. Additionally,
126 disruption of the interaction between I539 on the Jα helix and the LOV2 core partially unfolds the Jα
127 helix (41). These constraints together limit the amount of Jα sequence we can modify.

128 We tested a small battery of constructs for light-dependent myosin VI binding using our
129 mitochondrial recruitment assay (**Figure 1B**). One construct, which we refer to as LOVDab (**Figure 1C**),
130 exhibits robust recruitment of myosin VI in response to light (**Figure 1D**). As intended, Tom70^{helix}-FP-
131 LOVDab localizes to the surface of mitochondria, which are visible as puncta (**Figure 1D**). When the LOV2
132 is in the dark state, mCherry-myosin VI fluorescence shows a diffuse, cytosolic signature indicating that
133 it is unbound and diffuse throughout the cytosol. Upon LOV2 activation via whole cell illumination with a
134 blue, 488 nm laser, the myosin VI fluorescence is depleted from the cytosol and forms puncta
135 corresponding to the mitochondria where Tom70^{helix}-FP-LOVDab resides (**Figure 1D**). Thus, LOVDab
136 exhibits light-dependent binding to myosin VI.

137 Small deviations from this sequence abolish this light-dependent recruitment. LOVDab lacking K544
138 shows minor switching that was often accompanied with high dark state binding. LOVDab lacking both
139 A543 and K544 shows weak, constitutive binding, indicating that moving the Dab2^{pep} closer to the LOV2
140 domain beyond these residues destabilized the Jα helix. The insertion of residues either C-terminal to
141 K545 in the LOV2 sequence, or N-terminal to S678 in the LOVDab sequence, even when making
142 compensatory insertions or deletions in the opposite fusion protein to maintain the myosin VI CBD
143 binding site on the identical face of the Jα helix, prevents caging of Dab2^{pep}. Adding S678 of Dab2^{pep} to
144 LOVDab produced a construct with similar switching as LOVDab. Following the predicted register of the
145 helix, this fusion would position F680, a residue that is buried in the Dab2^{pep}:CBD interface (**Figure 1A**),

146 facing toward the Hβ-Iβ loop of LOV2. However, this construct shows a small level of dark state binding,
147 so we continued our study with LOVDab.

148 Both LOVDab and $LOVDab_{+ctrl}$ contain the double mutation T406A/T407A on the A'α helix. This
149 double mutation stabilizes the Jα helix by increasing the helicity of the neighboring A'α helix, which in
150 turn improves caging of peptides fused to the Jα helix (30, 36). Modeling using the crystal structure of
151 LOV2 and that of the $Dab2^{pep}{}_2$:CBD_2 complex suggests that LOVDab blocks $Dab2^{pep}$ from binding to the
152 CBD of myosin VI by sterically occluding the CBD from its binding site on $Dab2^{pep}$ (**Figure 1E**).
153 Interestingly, the largest steric clash is between the CBD and the A'α helix, suggesting that both terminal
154 helices contribute directly to the caging of $Dab2^{pep}$. In contrast, the flexible $Dab2^{pep}$ residues 674-679 in
155 $LOV2Dab^{pep}{}_{+ctrl}$ make this steric clash unlikely. This clash, together with the placement of $Dab2^{pep}$ F680 in
156 the LOV2 L546 position in LOVDab (42), may explain why this construct shows such robust light-
157 dependent recruitment.

158 We further probed the structural changes in LOVDab and $LOVDab_{+ctrl}$ using circular dichroism (CD) at
159 222 nm to interrogate the light triggered unfolding of the Jα helix and the uncaging of $Dab2^{pep}$. In order
160 to better replicate the protein used in the *in vivo* assays, we fused an EGFP to the N-termini of LOVDab
161 and $LOVDab_{+ctrl}$ for our CD measurements. The observed 25% fractional change in helicity in EGFP-
162 $LOVDab_{+ctrl}$ compares well with our previously measured values for the LOV2 domain (36), suggesting
163 that fusion to either EGFP or $Dab2^{pep}$ does not alter the extent of conformational change. We expect
164 that $Dab2^{pep}$ forms a helical extension of the Jα helix in LOVDab, whereas $Dab2^{pep}$ is likely unfolded in
165 EGFP-$LOVDab_{+ctrl}$, as $Dab2^{pep}$'s intrinsic helicity is only 0.64% (43). Consistent with this finding, the
166 fractional change in helicity is smaller in EGFP-LOVDab than in EGFP-$LOVDab_{+ctrl}$ (**Figure 1F**), in part
167 driven by the 20% higher intrinsic helicity of EGFP-LOVDab over EGFP-$LOVDab_{+ctrl}$. This decrease in
168 apparent unfolding of the Jα helix supports the notion that the $Dab2^{pep}$ is more tightly caged in LOVDab
169 than in $LOVDab_{+ctrl}$.

170 **Photoswitchable cargo recruits myosin VI to diverse membrane compartments in the cell.**

171 One benefit of optogenetic approaches is their ability to control proteins at a subcellular level. Using a
172 focused laser beam, myosin VI recruitment via LOVDab was performed selectively on subcellular regions
173 (<5 μm in diameter) in a reversible and repeatable manner (**Figures 2A-C, Video 1**). Overlaying the helix
174 recovery CD trace of LOVDab on the mitochondrial fluorescence (**Figures 2C**) shows that myosin VI
175 unbinds from the mitochondria at a similar rate to the Jα helix refolding in the dark, indicating that
176 myosin VI recruitment is occurring through our LOV2 construct.

177 To test the generalizability of this recruitment, we targeted LOVDab to two other membranes, the
178 plasma membrane. By fusing LOVDab to beta-2-adrenergic receptor (B2AR), we demonstrate
179 recruitment of myosin VI to the plasma membrane in response to light (**Figures 2D,E**, **Video 2**). The flat
180 shape of the HeLa cell makes it more challenging to observe the contrast in cytosolic versus membrane-
181 bound myosin VI as compared to that with mitochondria in the previous assay. Therefore, LOVDab is a
182 robust recruiter of myosin VI.

183

184 **Light-dependent recruitment of myosin VI stalls peroxisomes.**

185 Peroxisome movement is highly coupled to microtubule dynamics (44). Myosin V has previously
186 been shown to slow the redistribution of peroxisomes upon recruitment of constitutively active kinesin-
187 2, causing the peroxisomes to accumulate near the cell boundary. These observations suggest that
188 myosins are capable of stalling and/or decoupling peroxisomes from microtubule machinery (45). We
189 reasoned that if recruiting myosin VI to peroxisomes alters their motion inside the cell, this assay could
190 determine whether LOVDab can activate myosin VI upon its recruitment. We targeted LOVDab and
191 $LOVDab_{+ctrl}$ to peroxisomes by fusing the Pex3 membrane targeting domain ($Pex3^{MTD}$) to its N-terminus
192 (46). We find that among cells co-transfected with $Pex3^{MTD}$-FP-$LOV2Dab2^{pep}_{+ctrl}$ and myosin VI, cells

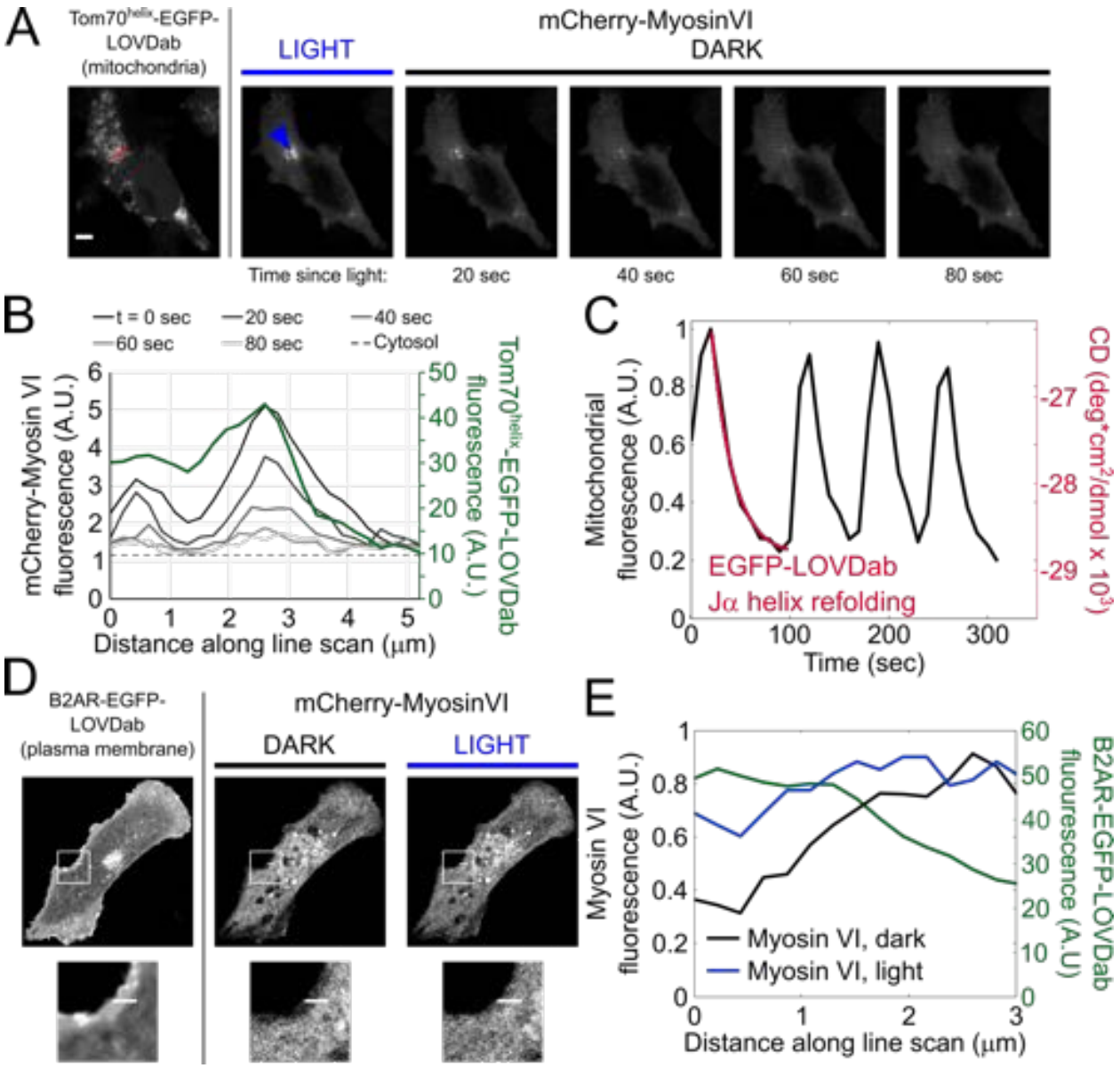

Figure 2. LOVDab robustly recruits myosin VI to different membranes within the cell in a light dependent manner. (**A-C**) Spot-specific, light-dependent recruitment of myosin VI to mitochondria. (**A**) Images of cell showing spot-dependent (blue arrow) recruitment of myosin VI. As cell is left in dark, myosin VI unbinds. Scale bar: 5 μm. (**B**) Fluorescence intensity line scan across red line in (**A**) over time. (**C**) Mean fluorescence in spot peak in (**A**) quantified over sequential pulses of light shows myosin VI recruitment is reversible and repeatable. Overlayed circular dichroism (CD) trace of EGFP-LOVDab photorecovery indicates that the myosin unbinding rate is similar to the refolding rate of the Jα helix in LOVDab. (**D**) Light-dependent recruitment of myosin VI to the plasma membrane. *Bottom row*: expanded view. Line is approximately 3 μm (see (**E**)). (**E**) Quantification of fluorescence of line in Panel (**D**). Fluorescence increases near cell edge where the plasma membrane is in focus.

193

194 having high myosin VI concentration exhibit constitutive binding between LOV2Dab2$^{pep}_{+ctrl}$ and myosin
195 VI. In contrast, wild type peroxisomes do not show significant binding of myosin VI (**Figures 3A,B**).
196 Significantly, peroxisomes that bind myosin VI have overall slower velocities than wild type peroxisomes,
197 supporting previous data showing that myosin V is capable of stalling microtubule-directed transport of
198 these organelles (45).

199 We next targeted LOVDab to peroxisomes, and were able to achieve reversible, light-dependent
200 recruitment of myosin VI to this organelle (**Figures 4A,B**; **Video 3**). Furthermore, the recruitment occurs
201 only to peroxisomes coated in LOVDab. Recruitment did not appear to be sufficient to deplete myosin VI
202 from other vesicles in the cell, suggesting that our design does not impact native myosin VI activity.

203 Lit peroxisomes move more slowly, presumably because the recruited myosin VIs act as a dynamic
204 tension sensor that stalls and anchors peroxisomes to the actin network (47). Reduced peroxisome
205 movement is evident from projections of maximum pixel values from consecutive blocks of 24-25
206 frames (46-48 seconds), as the fast moving peroxisomes form blurred patterns that coalesce into
207 compact puncta in the light (**Figure 4C**, **Video 4**). After three minutes in the dark, the peroxisome
208 motility resumes, as indicated by the blurred patterns reappearing. We therefore conclude that LOVDab
209 is capable of reversibly activating myosin VI *in vivo*.

210

211 **Activation of myosin VI in an *in vitro* gliding filament assay.**

212 Myosin VI could halt peroxisome movements by binding to actin filaments either with or without motor
213 activity. In order to directly demonstrate activation of myosin VI motility by Dab2^{pep}, we designed a
214 modified gliding filament assay whereby we anchor an EGFP-LOV2-Dab2^{pep} fusion protein to the surface
215 of a glass coverslip through an anti-GFP antibody (3E6). We then perfused soluble mCherry-myosin VI
216 with actin together (**Figure 5A**). This design allows us to interrogate myosin VI activation without
217 altering its C-terminal cargo binding domain.

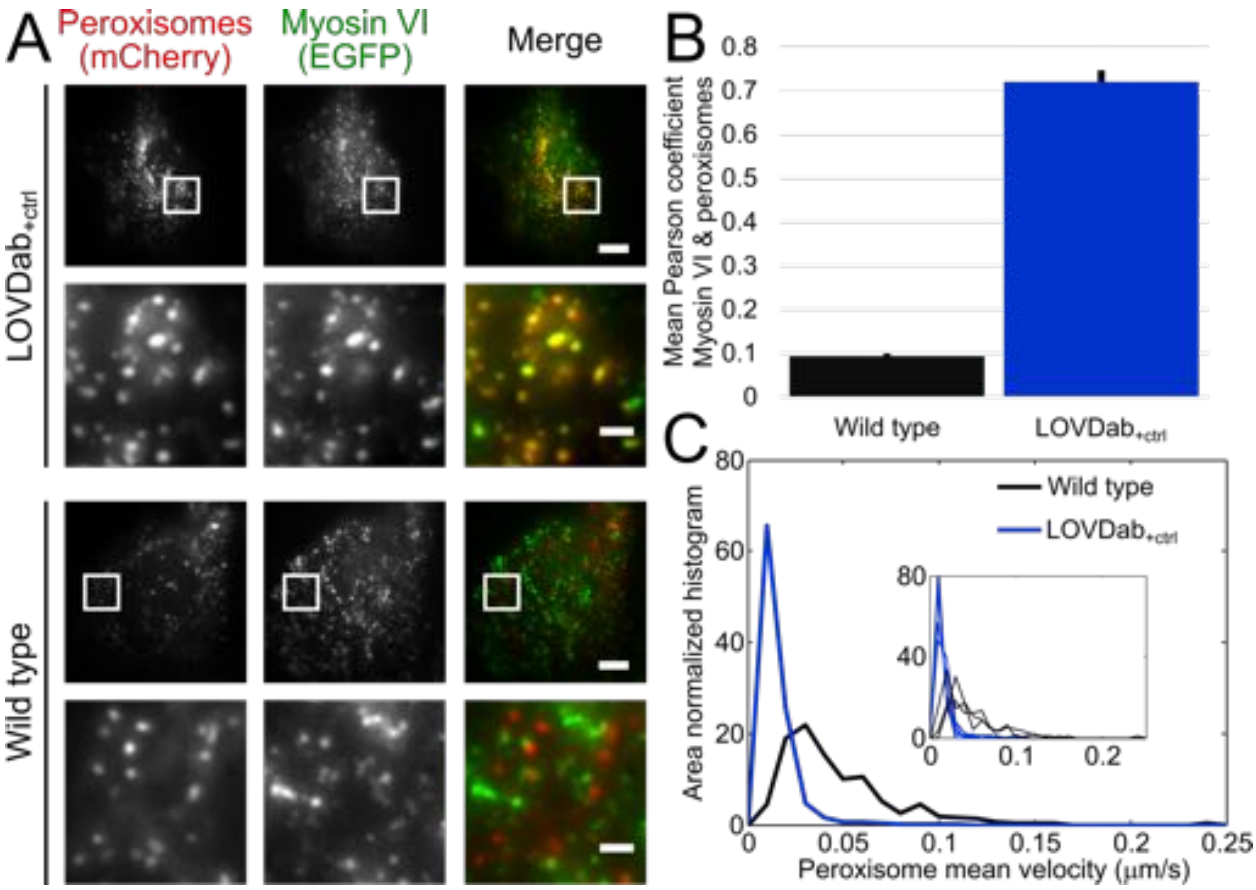

Figure 3. Myosin VI is recruited to peroxisomes via Dab2^{pep}. (**A**) The membrane targeting domain of Pex3 (Pex3^{MTD}) is used to express either mCherry-LOVDab$_{+ctrl}$ or mCherry only (Wild type). Top two rows: Cells with peroxisomes containing LOVDab$_{+ctrl}$ bind EGFP-myosin VI. Bottom two rows: Wild type peroxisomes lacking LOVDab$_{+ctrl}$ do not bind myosin VI. The 2nd and 4th rows are expanded views of boxed regions in the 1st and 3rd rows, respectively. Scale bars: 5 μm (1 μm expanded). (**B**) Quantification of overlap between peroxisome and myosin VI channels confirms significant recruitment of myosin VI to peroxisomes labeled with LOVDab$_{+ctrl}$ (mean ± SEM, $p << .01$, t-test; wild type, n=3; LOV2Dab2$^{pep}_{+ctrl}$, n=6). (**C**) Peroxisome frame-to-frame velocities are markedly reduced in cells expressing Pex3^{MTD}-mCherry- LOVDab$_{+ctrl.}$ Inset shows distributions for each cell used in analysis. Main graph shows distributions pooling all peroxisome data from these cells.

218

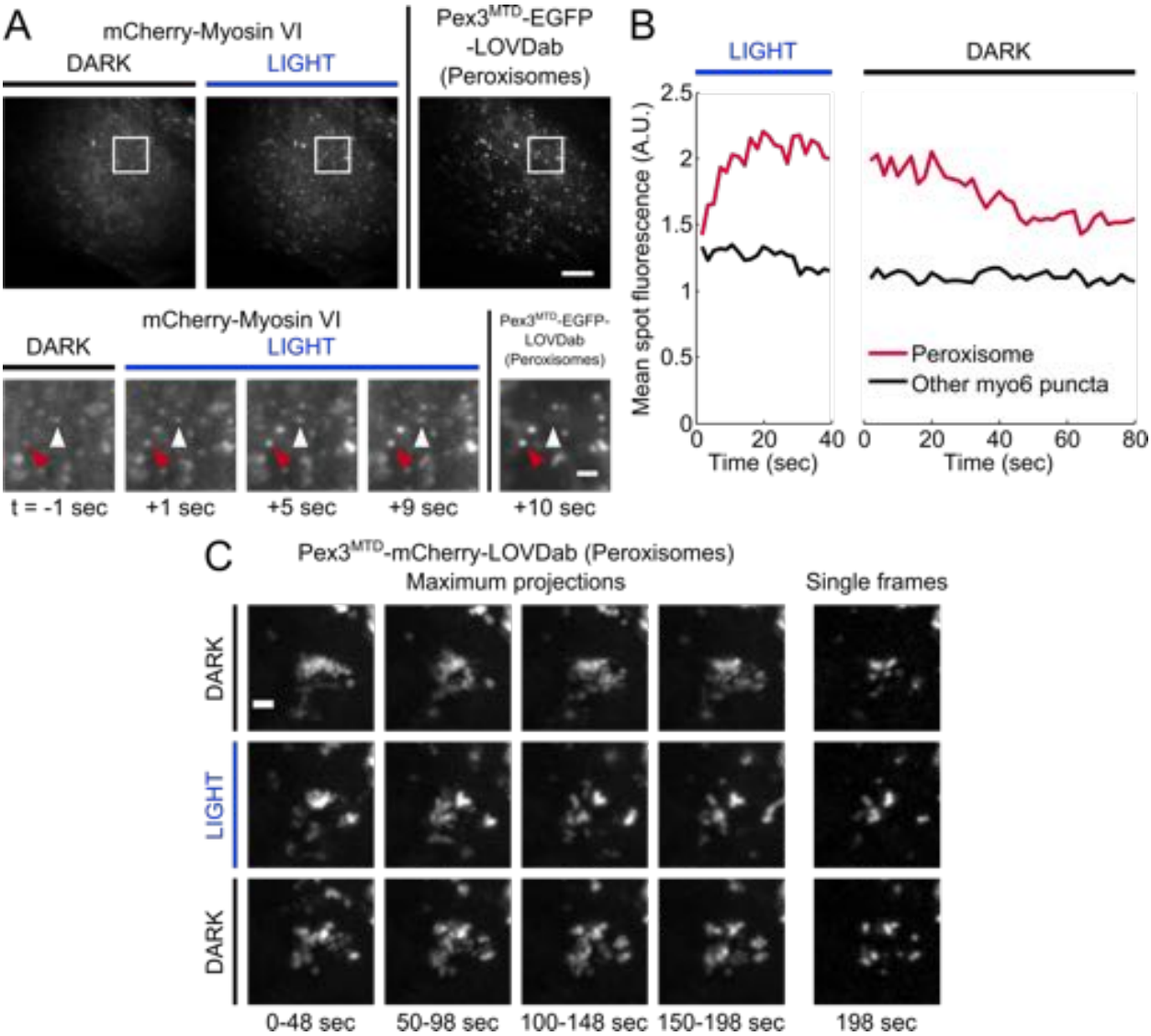

Figure 4. LOVDab reversibly recruits EGFP-myosin VI to peroxisomes in a light-dependent manner, which causes them to stall. (**A**) Images of cell showing light-dependent recruitment of myosin VI to peroxisomes. *Top row*: whole cell view. *Bottom row*: expanded image of boxed region. Vesicles showing light-dependent recruitment (red arrows) correspond to peroxisomes (right image) while vesicles binding myosin VI in the dark do not (white arrows). Thus, light-dependent recruitment occurs through LOVDab. Scale bars: 5 μm (1 μm expanded). (**B**) Quantification of fluorescence of vesicles labelled in (**A**). The red line corresponds to red arrowed vesicle; black line to the white labeled vesicle. (**C**) Maximum intensity projections over 48-50 seconds of peroxisome movement in a cell expressing EGFP-myosin VI and Pex3^{MTD}-mCherry-LOVDab. Peroxisomes moving diffusively appear blurred out and occupy expanded areas. Restricted peroxisomes occupy compact spaces (see right picture, middle row). As LOVDab is activated, peroxisomes stall, displaying more limited excursions. Motions resume after peroxisomes are left in the dark (3 minute delay between middle and bottom row). Projections constructed from consecutive blocks of 24-25 two second frames. Each row is from separate video; time increases down and to the right. Scale bar, 1μm.

219

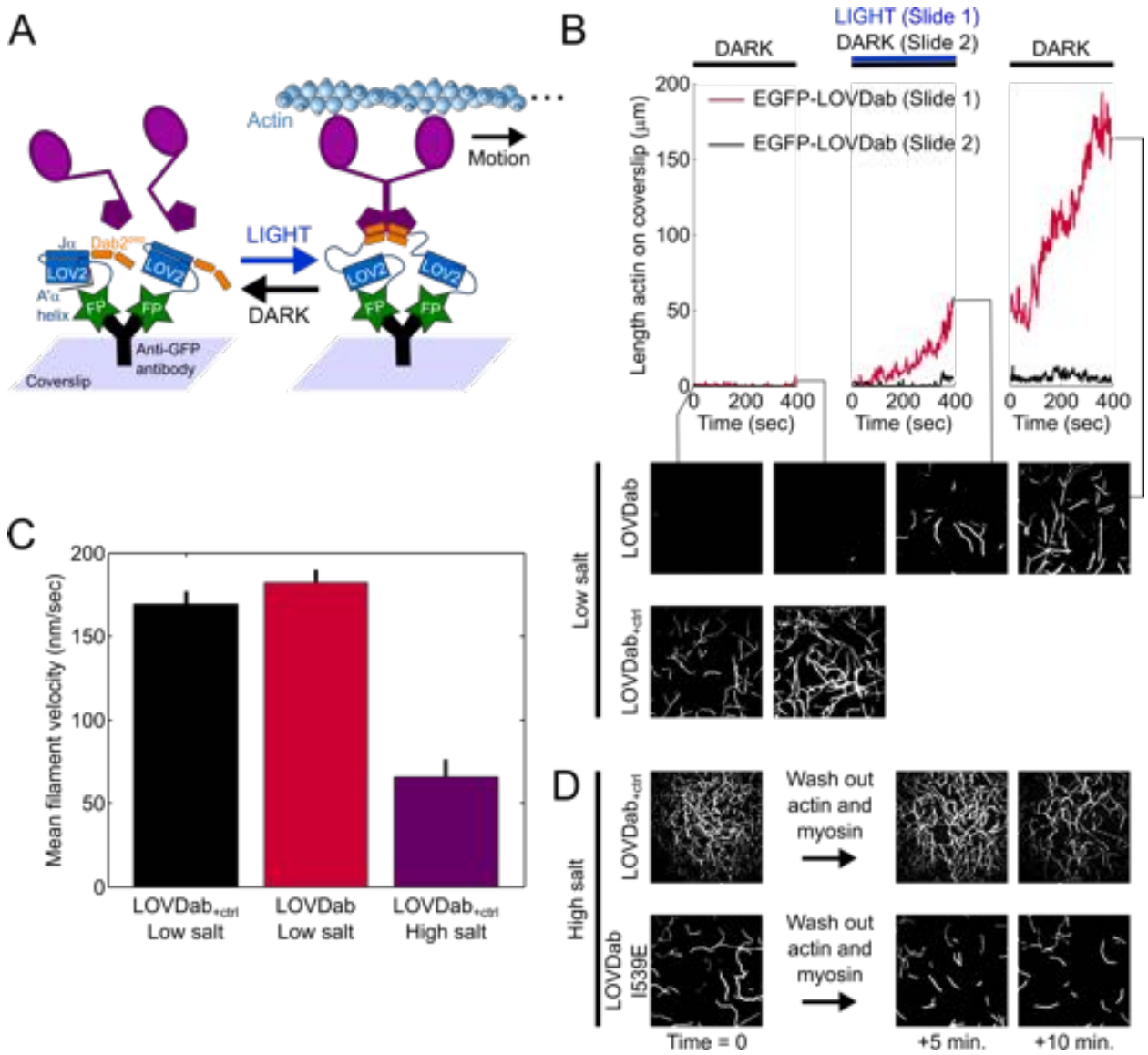

Figure 5. *In vitro* gliding filament assay indicates that LOVDab activates full-length human myosin VI in response to light. (**A**) Diagram of the modified gliding filament assay. EGFP-LOVDab is attached to the coverslip surface using an anti-GFP antibody. Soluble myosin VI is recruited to the surface by Dab2^{pep} and translates actin filaments. (**B**) Quantification of actin binding to surface over time for LOVDab. Recorded in multiple videos. Slide 1 was prepared and excited throughout second video. Slide 2 was left in the dark for all three recordings. Pictures underneath correspond to indicated time points in red curve. Below, matching time points for a representative slide coated with LOVDab$_{+ctrl}$ are included for comparison. (**C**) Filament velocities in different conditions. Salt significantly alters filament velocity while velocities for LOVDab and LOVDab$_{+ctrl}$ are similar (mean + SEM; first column, n=4; others, n=3). (**D**) *Upper row*: in high salt, actin releases from coverslip when free myosin and actin are washed out of the slide. *Lower row*: the I539E mutation unfolds the Jα helix, acting as a constitutive lit state mutant. This mutation allows LOVDab to recruit actin to the surface in high salt.

220

221 We find that full-length human myosin VI purified in a low salt ([KCl] = 25mM) MOPS buffer propels
222 filaments at 170 nm/sec when recruited by LOVDab$_{+ctrl}$. This velocity agrees well with published values
223 (12, 48). Under these conditions, LOVDab$_{+ctrl}$ recruits actin to the surface rapidly in the dark (**Figure 5B**,
224 lower panels; **Video 5**).

225 When the coverslip is coated with LOVDab, myosin VI only recruits actin to the surface after the
226 LOV2 is excited with blue light (**Figure 5B**, **Video 6**). After 400 seconds of excitation, the coverslip surface
227 is not yet saturated with actin, indicating that the actin deposits at a slower rate than with LOVDab$_{+ctrl}$-
228 coated coverslips. The velocity of the actin filaments recruited through LOVDab is similar to that of
229 filaments recruited through LOVDab$_{+ctrl}$ (**Figure 5C**). This latter finding suggests that both constructs fully
230 activate myosin VI. The slower deposition rate for LOVDab may be due to the lower availability of the
231 Dab2^{pep} in LOVDab over LOVDab$_{+ctrl}$, leading to fewer recruited myosin VI motors. It could also reflect the
232 selective recruitment of microaggregates of myosin VI by LOVDab, which would diffuse to the surface
233 more slowly than monomeric myosin VI (see below).

234 For both constructs, myosin VI appears to be recruited to the surface irreversibly, as once the LOV2
235 was activated, actin did not release from the slide (**Figure 5B**, lower panels). To determine whether this
236 irreversibility was due to the high affinity of Dab2^{pep} for the myosin VI CBD, we attempted to invert the
237 gliding filament assay to directly observe myosin VI walking on actin. However, we find that myosin VI
238 purified in low salt solutions forms soluble microaggregates which are visible as diffusing clusters in the
239 TIRF microscope. Testing a series of buffers, we find that myosin VI prepared in a high salt (KCl = 150
240 mM) Tris buffer does not form visible microaggregates. Myosin VI prepared in this second buffer is
241 active in the gliding filament assay when LOVDab$_{+ctrl}$ is on the surface. Consistent with a reduction in the
242 myosin:actin affinity in high salt, filaments recruited to the surface in this assay have a significantly
243 reduced velocity (**Figure 5C**). This myosin also did not perform in the TIRF assay, either because the
244 concentration needed to dimerize the myosin VI using cargo was prohibitively high for detection using

245 TIRF, or because of the well-documented decrease in affinity between myosins and actin in high salt
246 conditions (49, 50).

247 Unlike in low salt conditions, washing out free actin and myosin VI from the slide results in the slow
248 release of myosin VI from LOVDab$_{+ctrl}$ in high salt. (**Figure 5D**) Together, the high off-rate of myosin VI
249 from the mitochondria and the reversibility in the high salt myosin VI preparation suggest that the
250 irreversibility seen in the gliding filament assays using myosin VI prepared in low salt was primarily due
251 to the presence of myosin VI microaggregates. However, without the high avidity of the myosin VI
252 microaggregates, we do not observe recruitment of actin to the surface via LOVDab under high salt
253 conditions. We postulate that the lack of myosin VI recruitment to LOVDab *in vitro* is due to the
254 engineered caging effect of the LOV2 domain on Dab2^{pep} in the LOVDab construct. This effect could
255 weaken the effective K_D for binding of Dab2^{pep} to myosin VI to a point where even in the light, the
256 myosin VI cannot be recruited at concentrations where it is soluble in our high salt buffers. Alternatively,
257 the lifetime of the LOVDab:myosin VI:actin complex may be too short to propel the actin filaments.
258 Importantly, LOVDab containing an I539E point mutation that unfolds the Jα helix (41) constitutively
259 recruited actin in the presence of high salt myosin VI, proving that LOVDab is inherently capable of
260 activating myosin VI (**Figure 5D**).

261 We also tested whether a LOV2 domain fused to the myosin VI-binding residues (412-520) of
262 optineurin (OPTN) could activate myosin VI in our gliding filament assay. Though EGFP-LOV2-OPTN$_{(412-520)}$
263 migrates as a dimer in size exclusion chromatography (**Figure 5 – figure supplement 1**), it does not
264 activate myosin VI. Lack of activation is consistent with recent studies showing that the large insert in
265 the myosin VI tail domain, which is present in our construct, occludes the OPTN binding site (21).
266 Furthermore, OPTN must be ubiquitinated prior to binding myosin VI (20).

267 **Multiple signals contribute to myosin VI activation**

268 Other factors that may contribute to the differences in our *in vivo* and *in vitro* assays include the lack of
269 Ca^{2+} and PI(4,5)P_2 in the *in vitro* assays, both of which are known to bind myosin VI (23, 24). At myosin VI
270 concentrations too low to interact with LOVDab$_{+ctrl}$, the addition of PI(4,5)P_2 rescues recruitment of actin
271 to the coverslip (**Figure 6A**). This rescue requires the presence of Ca^{2+} ions, suggesting that the three
272 signals, PI(4,5)P_2, Ca^{2+} and Dab2, are integrated to activate myosin VI in the proper time and place in the
273 cell.

274 This signal integration could explain recruitment of myosin VI to the Golgi via LOVDab with the KDEL
275 receptor (KDELR). Overexpression of KDELR seems to be cytotoxic. At low expression levels KDELR-FP-
276 LOVDab recruits myosin VI to the Golgi apparatus in a light-dependent manner (**Figure 6B,C; Video 7**).
277 However, the amount of myosin VI binding to each LOVDab-labeled membrane does not correlate with
278 the amount of LOVDab on that membrane (**Figure 6B-D**). This lack of correlation cannot be explained by
279 limiting myosin VI since when light is applied to the cell, additional myosin VI binds to each membrane.
280 Thus, other factors on these membranes must alter the myosin VI affinity for its protein cargo Dab2^{pep},
281 even between similar membranes. Together, these data support a new model of myosin VI activation
282 whereby myosin VI integrates multiple cargo signals to deploy in a site-specific manner in the cell
283 (**Figure 6E**, see discussion below). The presence of these signals *in vivo* also may explain why myosin VI is
284 activated by LOVDab *in vivo* but not in our *in vitro* gliding filament assay.

285 Discussion

286 Myosin VI is the only myosin that walks toward the pointed end of actin filaments (5, 6). This property
287 gives it many unique roles throughout the cell including endocytosis, cell migration, and autophagy (51).
288 Furthermore, the mechanism for myosin VI activation is still highly debated (13). To create a tool that
289 could help address these questions, we engineered an optogenetic activator of myosin VI, LOVDab.

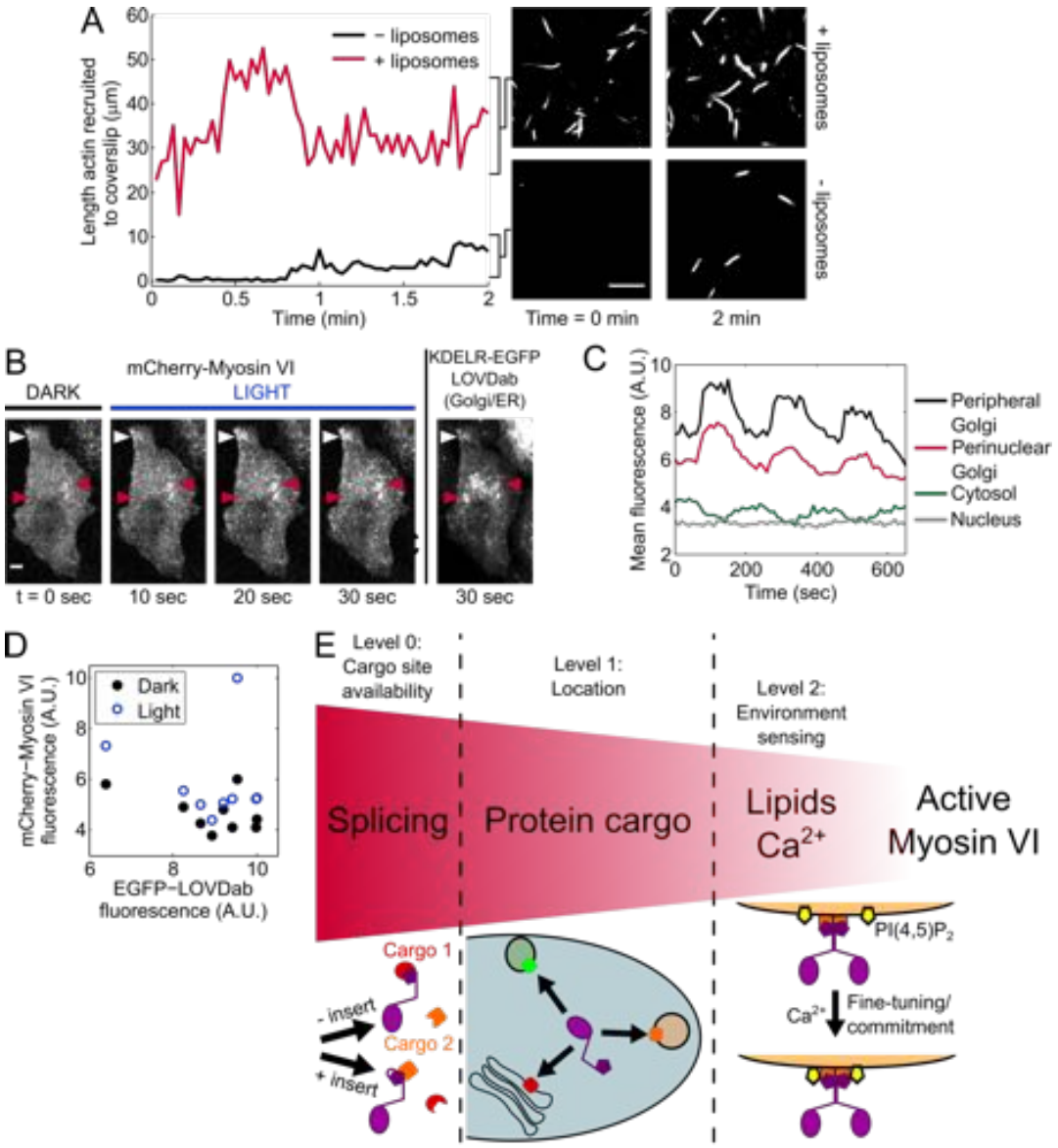

Figure 6. Myosin VI integrates cargo signals to deploy in site-specific manner. (**A**) At concentrations of mCherry2B-Myosin VI (prepared in physiological KCl conditions, see text) too low for $LOVDab_{+ctrl}$ to recruit actin to the coverslip (- liposomes, bottom), addition of artificial liposomes containing 5% $PI(4,5)P_2$ sensitizes full-length myosin VI to $Dab2^{pep}$ cargo, rescuing recruitment of actin to the surface (+ liposomes, top). (**B**) LOVDab was targeted to the Golgi apparatus using a KDEL receptor (KDELR) with an R5Q/D193N double mutation to promote retention in the Golgi. White arrows highlight peripheral Golgi that exceptionally recruits myosin VI. Red arrows highlight portions of perinuclear Golgi stacks, some of which recruit myosin VI well (right arrow) whereas others have minor switching (left arrow). Scale bar: 5μm. (**C**) Mean fluorescence in different areas of the cell described in (**B**). Perinuclear Golgi fluorescence is the mean of all perinuclear stacks. Cytosolic fluorescence is anticorrelated with Golgi fluorescence, indicating depletion of myosin VI from the cytosol upon excitation of LOVDab. Nuclear fluorescence is static and indicates the noise level of the measurement. (**D**) The amount of myosin VI binding is not correlated with the amount of LOVDab on the different Golgi stacks, indicating other factors in the cell must alter the myosin VI:LOVDab affinity on the different membranes. (**E**) Model of myosin VI cargo integration in the cell. Alternative splicing biases myosin VI isoforms to different cargo proteins. Protein cargo recruits myosin VI isoforms to specific locations in the cell and determines its oligomeric state. Lipid, Ca^{2+}, and other cargoes help myosin VI sense the environment, modulating its affinity for cargo, as seen in (**A-D**).

290

291 Previous optogenetic efforts to control motors recruited constitutively active, truncated, forced-dimer
292 motor proteins (52, 53). These designs provide an excellent means of laser-induced force-generation *in*
293 *vivo*, and allow researchers to use members of each of the three classes of motor proteins. Our LOVDab
294 differs in that it controls myosin VI through its native activation mechanism without any alterations to
295 the myosin itself. Thus, our approach allows for direct tests of myosin VI function and control in cellular
296 contexts. Additionally, since full-length myosin VI is auto-inhibited when not bound to cargo, our
297 method couples recruitment and motor activity, preventing potential adverse effects on cytoskeletal
298 systems when exogenous myosin VI is expressed *in vivo*.

299 Curiously, LOVDab places the residue F680 of $Dab2^{pep}$ (res. 674-711) in the L546 position of LOV2,
300 which Guntas *et al* observed to bind to a hydrophobic pocket in the non-FMN binding face of the β sheet
301 of LOV2 (42). When optimizing their LOV2-based recruitment system, "improved Light Inducible Dimer
302 (iLID)", they noticed their optimal switch had a key phenylalanine residue that bound this pocket.
303 Another parallel between our designs is a shortened photorecovery time. Their optimal construct
304 exhibits a photorecovery time with $\tau \approx 22$ seconds relative to the wild type value of 80 seconds (36).
305 Similarly, LOVDab exhibits a $\tau = 15$ seconds compared to $LOVDab_{+ctrl}$ which has a mean $\tau = 47$ seconds,
306 much closer to the recorded value for LOV2 406A/407A of 56 seconds (37). The relative difference in
307 photorecovery times are evident from the rates of Jα helix reversion in **Figure 1D**. Given the relative
308 intolerance of LOVDab to deviations of F680 from this position, these results suggest that this
309 hydrophobic pocket may be of general importance for caging peptides on the C-terminus of LOV2.
310 Furthermore, a quickened dark state reversion time may highlight a key role of the L546 pocket in the
311 overall conformational dynamics of the LOV2 domain. In any case, it seems that placing the $Dab2^{pep}$
312 F680 in this pocket contributed to robust, light-dependent recruitment of myosin VI by LOVDab.

313 We demonstrated that LOVDab is capable of recruiting myosin VI in a light-dependent manner to
314 mitochondrial, plasma, Golgi and peroxisomal membranes. Strictly speaking, however, binding of

315 myosin VI to Dab2^{pep} is not equivalent to activation. Activation requires the release of autoinhibition of
316 full-length myosin VI, allowing it to interact with actin in either a transport (54) or anchoring role (18). In
317 order to demonstrate activation of myosin VI *in vivo*, we showed that myosin VI recruited to
318 peroxisomes via our engineered positive control construct LOVDab$_{+ctrl}$ stalls these organelles. Similarly,
319 upon activation with light, LOVDab reversibly recruits myosin VI at high concentrations in the cell,
320 stalling peroxisomes. These findings indicate that upon recruitment by LOVDab, myosin VI is capable of
321 interacting with actin strongly enough to decouple peroxisomal motion from the underlying
322 microtubule-based processes that drive their native behavior (44). This anchoring strongly suggests that
323 LOVDab is capable of activating myosin VI *in vivo*.

324 In order to verify activation of myosin VI directly, we developed a modified *in vitro* gliding filament
325 assay in which myosin VI is recruited to the coverslip via LOVDab or LOVDab$_{+ctrl}$. Myosin VI purified
326 under either high or low salt conditions is active when recruited through LOVDab$_{+ctrl}$. Moreover, at low
327 concentrations of myosin VI, PI(4,5)P_2 -containing liposomes enhance myosin VI's affinity for LOVDab$_{+ctrl}$
328 (**Figure 6A**). Therefore, membranes enriched in PI(4,5)P_2 (55) would enhance myosin VI's effective
329 affinity to its cargo protein Dab2^{pep}. This enhancement requires Ca^{2+}, supporting recent studies
330 suggesting that Ca^{2+} transients could play a role in regulating myosin VI function (23, 24). Moreover,
331 when LOVDab is targeted to the Golgi apparatus, the amount of myosin VI bound does not scale with
332 the amount of LOVDab on a given stack. Therefore, local differences modulate myosin VI's ability to bind
333 these organelles. One cause for this difference could be in the concentrations of PI4P on the different
334 stacks. Though myosin VI binds more strongly to PI(4,5)P_2, it also shows significant binding to PI4P (23),
335 which is found on the Golgi (55). Another source of diversity is likely in Ca^{2+} transients, as secretory
336 pathway organelles such as the Golgi are rich in Ca^{2+} (56). The cisternae in the Golgi have different
337 luminal Ca^{2+} concentrations based on their developmental stage and can differentially release Ca^{2+} (57).

338 Together with our work, these data suggest that even within a cell, myosin VI integrates protein, lipid,
339 and Ca^{2+} signals to perform its function in a site-specific manner.

340 Our findings therefore support a new model of myosin VI activation where, rather than having a
341 given cargo for a given function, myosin VI integrates multiple signals on a given membrane to modulate
342 binding and motor activation (**Figure 6E**). Regulation through splicing biases myosin VI to certain protein
343 cargo adaptors (21). The protein cargos regulate the localization of myosin VI in the cell, and may also be
344 the primary determinant of myosin VI's oligomeric state (4). Once on-site, secondary cargo signals such
345 as lipids or Ca^{2+} may fine-tune myosin VI's activity at that location by increasing myosin VI's effective
346 affinity for its substrate, driving local activation (24).

347 LOVDab is a unique optogenetic tool in that it activates full-length myosin VI without altering the
348 myosin itself, allowing for direct inferences on myosin VI activity and regulation *in vitro* and *in vivo*. Our
349 approach here could guide similar optogenetic efforts to control native systems with minimal
350 perturbation. LOVDab exhibits robust, light-dependent myosin VI recruitment to many different
351 organelles, and myosin binding to LOVDab propels actin filaments in vitro. Using LOVDab, we discovered
352 evidence for a new activation model for human myosin VI, whereby myosin VI integrates its activation
353 signals to obtain a site-specific mode of activation. How each of these cargos are integrated, and how
354 this integration is reflected structurally in myosin VI, are outstanding questions. In particular, the
355 relation between the oligomeric state of myosin VI and its site-specific roles in the cell, and how this is
356 impacted by different cargos, is not entirely known. We believe that LOVDab will be an extremely useful
357 tool for answering these and additional questions about how this important motor protein functions in
358 the cell.

359 # Materials and methods

360 **Plasmid construction**

361 For protein purification, plasmids encoding LOV2-Dab2^{pep} fusion proteins were engineered within a
362 pHISparallel1 vector encoding a modular -/NdeI/-His6-Protein G-/AgeI/-EGFP-/EcoRI/-LOV2-Dab2^{pep}-
363 /XhoI/- that allowed for facile swapping of domains via ligation. Full-length myosin VI was incorporated
364 into baculovirus for expression in SF9 cells using the BestBac system by Expression Systems (Nevada,
365 USA) according to the manufacturer's guidelines. An mCherry2B (58) with an N-terminal FLAG tag was
366 first incorporated at the myosin VI N-terminus within the pET vector (see below) prior to insertion into a
367 modified pBlueBac plasmid via SLiCE cloning due to the large sizes of the fragments (59). We fused
368 mCherry2B to its to improve solubility, reduce dimerization, and increase fluorescence of the protein
369 over mCherry (58).

370 For live cell imaging, LOV2-Dab2^{pep} plasmid constructs were created for transfection using ligations
371 from a modular pEGFP vector containing the general sequence -/NheI/-membrane tag-/AgeI/-FP-
372 /EcoRI/-LOV2-Dab2^{pep}-/BamHI/- Membrane tags include: for mitochondria, the mitochondrial outer
373 membrane targeting sequence of yeast Tom70^{helix} (res. 1-40); for the plasma membrane, full length
374 golden hamster Beta-2-Adrenergic Receptor (B2AR); for the Golgi Apparatus, full-length human KDEL
375 receptor containing a R5Q/D193N double mutation to improve retention in the Golgi (60, 61); and for
376 peroxisomes, the N-terminal targeting sequence of human Pex3 (res. 1-42) (Pex3^{MTD}) with a (GGS)x3
377 linker (46, 62). Tom70^{helix} and B2AR were generous gifts from M. Glotzer. KDELR and Pex3^{MTD} were
378 constructed from gBlocks ordered from Integrated DNA Technologies (Coralville, IA). Full-length human
379 myosin VI, isoform 1 (a generous gift from M. Zhang) was expressed in their modified pET vector
380 containing a sequence encoding -/NheI/-FP-/XhoI/-myosin VI-/NotI/-. Fluorescent proteins were
381 exchanged via ligation.

382 **Protein purification**

383 LOV2-containing constructs were purified as described previously (36). Briefly, constructs were
384 expressed in E. coli with an $(His)_6$-Protein G fusion to their N-terminus, followed by a TEV protease
385 restriction site. After elution from the Ni-NTA column, proteins were dialyzed against a TEV protease
386 cleavage buffer (50 mM Tris, 1 mM EDTA, 1 mM DTT, pH = 8.0) before or during the cleavage reaction.
387 EDTA and DTT were removed by dialysis prior to passing the cleaved protein through a regenerated Ni-
388 NTA column. Proteins were then concentrated and ran on a size exclusion column (HiPrep 16/60 S-100
389 HR, GE Healthcare Life Sciences) that was equilibrated in the relevant assay buffer.

390 Full-length human myosin VI with an N-terminal FLAG-mCherry2B fusion was incorporated into
391 baculovirus as discussed above. SF9 cells were infected at a 1:1 MOI and proteins were harvested from
392 SF9 cells 58-72 hours post infection. The cells were re-suspended in Lysis buffer (see below for recipes)
393 containing 2 mM ATP, and a cocktail of protease inhibitors including 1mM phenylmethylsulfonyl fluoride
394 (PMSF) and 10μg/mL each of: aprotinin, leupeptin, chymostatin, and pepstatin A. The cells were lysed by
395 douncing and nutated for 40 minutes at $4^{o}C$ to allow the myosin VI to diffuse out of the cells. The lysate
396 was spun at 14,000 rpm in a Legend X1R centrifuge (F15S-8x50c rotor, Thermo Scientific) and a variable
397 amount of anti-FLAG resin (M2, Sigma) added to the supernatant. After incubation, the resin was spun
398 out of suspension at 900xg in a 5810R centrifuge (A-4-81 rotor, Eppendorf) and washed with wash
399 buffer (see below) containing 3 mM ATP, a variable amount of Calmodulin, and protease inhibitors.
400 Resin was repelleted using the same procedure and re-suspended in wash buffer before transferred to a
401 drip column where the resin was further washed. Resin was then incubated with elution buffer (wash
402 buffer + 0.2 mg/mL FLAG peptide) for 1 hour. Protein was eluted and dialyzed against wash buffer
403 containing no ATP or protease inhibitors. In the low salt preps (see text) the lysis buffer was 50 mM
404 Tris·HCl, 150 mM KCl, 0.5 mM DTT, and 0.1% Triton X-100, pH = 7.7. The wash buffer was 20 mM
405 imidazole, 150 mM KCl, 5 mM $MgCl_2$, 1 mM EDTA, and 1 mM EGTA, and 0.5 mM DTT, pH = 7.5. The

406 storage/dialysis buffer was either AB: 25mM imidazole, 25 mM KCl, 4 mM Mg_2Cl_2, 1mM EGTA, 2mM
407 DTT, pH = 7.5; or KMg25: 10 mM MOPS, 25 mM KCl, 1 mM EGTA, 1 mM $MgCl_2$, and 1 mM DTT, pH = 7.0.
408 For the high salt prep, the lysis buffer was 50 mM Tris·HCl, 150 mM KCl, 0.5 mM EDTA, 1 mM EGTA, 4
409 mM $MgCl_2$, 0.5 mM DTT, and 0.1% Triton X-100, pH = 7.3, and the final dialysis/assay buffer was 50mM
410 Tris·HCl, 150 mM KCl, 1 mM EDTA, 1mM EGTA, 5 mM MgCl2, and 0.5 mM DTT (1 mM DTT for final
411 dialysis), pH = 7.3. For both preps, buffers were chilled to 0-4°C before use. pH values were set at room
412 temperature.

413 Protein purity was assessed using SDS-PAGE. In the case of LOV2-containing constructs, protein
414 quality was further assessed using UV-Vis spectroscopy to measure the FMN photorecovery rate and
415 circular dichroism (CD) (see below) to measure the fractional change in helicity of the protein, as done
416 previously in our lab (36). The UV-Vis spectroscopy was carried out on an Olis HP 8452 Diode Array
417 Spectrophotometer (Bogart, GA). The recovery of FMN absorbance at 448 nm was fit to a single
418 exponential using MATLAB to obtain the FMN dark state recovery time constant, τ_{FMN}. Circular dichroism
419 (CD) was performed on a Jasco 715 spectrophotometer and a 40W white LED lamp (BT DWNLT A,
420 TheLEDLight.com) was used to excite the LOV2 domain in the cuvette for ≥ 12 seconds for photo
421 excitation. The refolding traces at 222 nm were fit to a single exponential using MATLAB and the
422 fractional change in helicity in the protein as $\delta_{222} = (CD_{222,dark}-CD_{222,light})/CD_{222,dark}$.

423 **Gliding filament assay**

424 Nitrocellulose-coated coverslips were first coated in anti-GFP antibody (clone 3E6 MP Biomedicals,
425 California, USA) at 0.25 μg/mL in PBS. Following this, coverslips were blocked using 1 mg/mL BSA (ELISA
426 grade, EMD Millipore) and the antibody saturated using EGFP-LOV2-Dab2^{pep} at 1 μM. After this, the slide
427 was washed using KMg25 and a solution containing myosin VI, F-actin, and an oxygen scavenging system
428 (0.45% glucose (w/v) 0.5% (v/v) BME, 432 μg/mL glucose oxidase, and 72 μg/mL catalase) (63) was
429 perfused. Slides were then imaged using an x100, 1.65 NA objective (Olympus) on a custom-built total

430 internal reflection microscope employing an EMCCD camera (iXon; Andor Technologies). This
431 microscope was controlled with the open source Micro-Manager program (www.micro-manager.org).
432 For assays involving lipid cargo, artificial liposomes from Echelon Biosciences (Utah, USA) containing 5%
433 of the signaling lipid PI(4,5)P_2 were added to the assay buffer. The liposomes had no effect on myosin VI
434 activity if Ca^{2+} was not present at a total concentration of at least 1.5 mM (corresponding to a free Ca^{2+}
435 concentration of approximately 25 μM). The necessity of Ca^{2+} matches previous results but this
436 concentration is approximately tenfold lower than previously used for assessing the interaction of lipids
437 with the myosin VI tail domain (23).

438 Gliding filament velocities were calculated from at least 3 videos from at least 2 independent
439 preparations of myosin VI, using at least 10 filaments/video and at least 10 frames/filament. MTrackJ
440 was used to generate the actin tracks (64). Filaments showing smooth and continuous movement were
441 tracked. To quantify the length of actin on the coverslip, images were background subtracted and
442 thresholded to create binary images of the actin that were then skeletonized using the ImageJ function.
443 The sum of pixels in the images were converted to length using the pixel calibration and used as the
444 estimate for the length of actin on the coverslip.

445 **Live cell assays**

446 HeLa cells were passaged in Dulbecco's modified Eagle medium (DMEM) from Corning (New York, USA)
447 supplemented with 10% heat-inactivated FBS (Sigma, Missouri, USA) and 1x HyClone pen-strep-L-glut
448 (GE Healthcare Life Sciences, Utah, USA). One day prior to transfection, cells were split onto plasma
449 cleaned glass coverslips. Coverslips that were 80-95% confluent were washed into DMEM media lacking
450 supplements 10-20 minutes prior to transfection. Cells were co-transfected with a combination of
451 plasmids containing genes for either an FP-LOV2-Dab2^{pep} construct fused to a gene encoding an
452 organelle-targeting transmembrane protein at its 5' end or a gene encoding full-length human myosin VI
453 with either EGFP or mCherry2B (see above) at its N-terminus using Lipofectamine 2000 (Life

454 Technologies, Illinois, USA), according to the manufacturer's guidelines. Cells were imaged 18-24 hours
455 post-transfection. Confocal images were taken using a 63×, 1.4 numerical aperture (NA) objective on an
456 Axiovert 200M microscope (Zeiss) with a spinning disk confocal (CSU10, Yokogawa) and an electron-
457 multiplying charge-coupled device (EMCCD) camera (Cascade 512B, Photometrics). The microscope was
458 controlled using MetaMorph (Molecular Devices). TIRF images (peroxisome experiments) were taken
459 using the microscope used in the gliding filament assay. Videos were background subtracted using either
460 the rolling ball or parabolic algorithms in ImageJ (65). Quantified pixel values are plotted post-
461 background subtraction to match images shown.

462 **Author Contributions**

463 ARF, TRS and RSR designed research; ARF performed research and analyzed data, ARF, TRS and RSR
464 wrote the manuscript.

465 **Acknowledgments**

466 The authors thank Michael Glotzer and Margaret Gardel for sharing equipment, and members of the
467 Sosnick and Rock labs for helpful discussions. This work was supported by NIH R01s GM078450/S1 and
468 GM109863 (to RSR), GM55694 (to TRS) and NIH T32 GM007183 (to B. Glick).

469 **SUPPORTING INFORMATION**

470

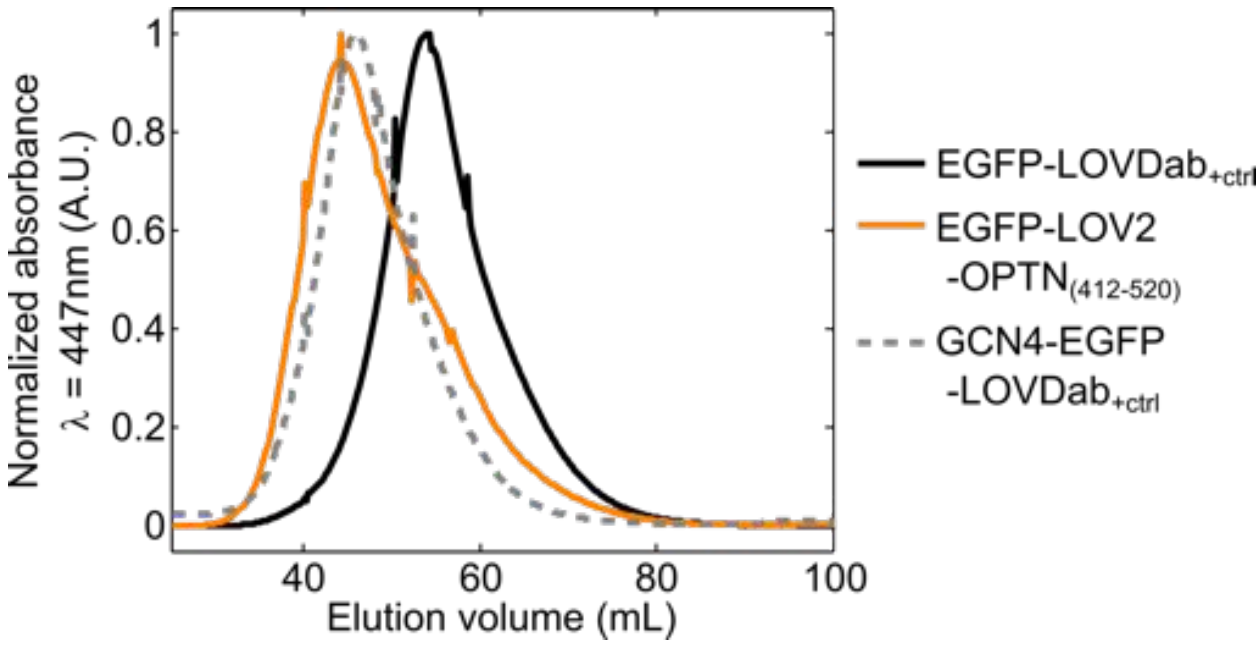

Figure 5-figure supplement 1. EGFP-LOV2 fused to the myosin VI-binding portion of Optineurin migrates as a dimer by size exclusion chromatography. Optineurin (OPTN) has previously been shown to activate full-length porcine myosin VI at much lower concentrations than a truncated portion of Dab2 containing $Dab2^{pep}$ (4). We therefore wanted to test whether the putative myosin VI binding site on OPTN (res. 412-520) could activate full-length human myosin VI in our gliding filament assay. Comparison to the elution trace of EGFP-$LOVDab_{+ctrl}$ dimerized via a GCN4 leucine zipper, $OPTN_{(421-520)}$ fused to the C-terminus of EGFP-LOV2 migrates as a dimer in our size exclusion column. This is consistent with previous reports showing OPTN is a dimer (4) and the prediction that these residues in OPTN form a coiled-coil (14, 15). However, EGFP-LOV2-$OPTN_{(412-520)}$ did not recruit actin to the surface of our gliding filament assay, seemingly inconsistent with the study showing activation of porcine myosin VI via optineurin. (4). Though OPTN binding to the myosin VI tail was shown to be large insert independent (19), one difference between porcine myosin VI and our human full length construct is that our construct contains the large insert of isoform 1. Since doing this experiment, a group of researchers have shown that myosin VI binds OPTN only after it has been ubiquitinated (20), and have solved the structure of a molecular "switch" region in the tail domain involving the long insert that occludes the OPTN binding site (21). Our results therefor support their findings.

471

472 **VIDEOS**

473 **Video 1.** Spot-specific recruitment of myosin VI to mitochondria. Two concatenated videos showing
474 subcellular recruitment of myosin VI to mitochondria in cell depicted in **Figure 2A**. Scale bar: 5 μm; time
475 stamp: min:sec.

476

477 **Video 2.** Light-dependent recruitment of myosin VI to plasma membrane. Plasma membrane is in focus
478 near cell edge (compare to **Figure 2D,E**). As cell is illuminated, myosin VI appears to spread from the
479 middle of the cell outwards, indicating binding to LOVDab on plasma membrane. Scale bar: 10 μm.

480

481 **Video 3.** Myosin VI is recruited to peroxisomes in a light-dependent manner. Sequential movies showing
482 light-dependent recruitment of myosin VI to peroxisomes in cell shown in **Figure 4A**, with subsequent
483 release of myosin VI in the dark. Scale bar: 5 μm. Time resets to 0 sec at the start of each video.

484

485 **Video 4.** Recruitment of myosin VI to peroxisomes causes them to stall. As light is applied to the cell
486 (**Figure 4C**), peroxisome movements slow. When the cell is returned to the dark, the peroxisomes begin
487 to move freely again. In the upper right, tubules are visible that occur in some cells overexpressing
488 peroxisome proteins. Tubules form independently of $Dab2^{pep}$. Scale bar: 5μm. Time stamp is min:sec and
489 resets to zero at the start of each movie; cell was left in the dark three minutes prior to final movie.

490

491 **Video 5.** Myosin VI bound to $LOVDab_{+ctrl}$ propels filaments in vivo. Gliding filament assay depicted in
492 **Figure 5A** with $LOVDab_{+ctrl}$. Video shows actin filaments propelled by myosin VI prepared in low salt,
493 indicating activation of myosin VI motor activity by $LOVDab_{+ctrl}$. Scale bar: 5μm; time stamp: min:sec.

494

495 **Video 6.** Light-dependent recruitment of actin to coverslip. Gliding filament assay depicted in **Figure 5A**
496 with LOVDab shows that once light is applied to the slide, actin filaments begin to come down to the
497 surface, indicating binding. However, actin filaments do not unbind from the coverslip when the slide is
498 returned to the dark. This differs from our *in vivo* experiments where myosin VI rapidly unbinds from the
499 membrane once the cell is returned to the dark (see **Figures 2A-C, 4B**; **Videos 1-3**). Scale bar: 5 μm; time
500 stamp: min:sec.
501
502 **Video 7.** Light-dependent recruitment of myosin VI to the Golgi apparatus. LOVDab targeted to Golgi
503 apparatus via KDEL receptor (R5Q/D193N) rapidly recruits myosin VI in the light and releases it in the
504 dark. Comparison to LOVDab channel (**Figure 6B-D**) shows that myosin VI binding is not proportional to
505 the amount of LOVDab on each Golgi stack. Scale bar: 5 μm; time stamp: min:sec.

506 **REFERENCES**

507 1. Gautier A, Gauron C, Volovitch M, Bensimon D, Jullien L, Vriz S. How to control proteins with
508 light in living systems. Nat Chem Biol. 2014;10(7):533-41.

509 2. Fenno L, Yizhar O, Deisseroth K. The development and application of optogenetics. Annu Rev
510 Neurosci. 2011;34:389-412.

511 3. Tischer D, Weiner OD. Illuminating cell signalling with optogenetic tools. Nat Rev Mol Cell Biol.
512 2014;15(8):551-8.

513 4. Phichith D, Travaglia M, Yang Z, Liu X, Zong AB, Safer D, et al. Cargo binding induces dimerization
514 of myosin VI. Proc Natl Acad Sci U S A. 2009;106(41):17320-4.

515 5. Wells AL, Lin AW, Chen LQ, Safer D, Cain SM, Hasson T, et al. Myosin VI is an actin-based motor
516 that moves backwards. Nature. 1999;401(6752):505-8.

517 6. Rock RS, Rice SE, Wells AL, Purcell TJ, Spudich JA, Sweeney HL. Myosin VI is a processive motor
518 with a large step size. Proc Natl Acad Sci U S A. 2001;98(24):13655-9.

519 7. Buss F, Arden SD, Lindsay M, Luzio JP, Kendrick-Jones J. Myosin VI isoform localized to clathrin-
520 coated vesicles with a role in clathrin-mediated endocytosis. EMBO J. 2001;20(14):3676-84.

521 8. Self T, Sobe T, Copeland NG, Jenkins NA, Avraham KB, Steel KP. Role of myosin VI in the
522 differentiation of cochlear hair cells. Dev Biol. 1999;214(2):331-41.

523 9. Warner CL, Stewart A, Luzio JP, Steel KP, Libby RT, Kendrick-Jones J, et al. Loss of myosin VI
524 reduces secretion and the size of the Golgi in fibroblasts from Snell's waltzer mice. EMBO J.
525 2003;22(3):569-79.

526 10. Tumbarello DA, Waxse BJ, Arden SD, Bright NA, Kendrick-Jones J, Buss F. Autophagy receptors
527 link myosin VI to autophagosomes to mediate Tom1-dependent autophagosome maturation and fusion
528 with the lysosome. Nat Cell Biol. 2012;14(10):1024-35.

529 11. Heissler SM, Sellers JR. Various Themes of Myosin Regulation. J Mol Biol. 2016;428(9 Pt B):1927-
530 46.
531 12. Lister I, Schmitz S, Walker M, Trinick J, Buss F, Veigel C, et al. A monomeric myosin VI with a
532 large working stroke. EMBO J. 2004;23(8):1729-38.
533 13. Sweeney HL, Houdusse A. Myosin VI rewrites the rules for myosin motors. Cell.
534 2010;141(4):573-82.
535 14. Kachaner D, Genin P, Laplantine E, Weil R. Toward an integrative view of Optineurin functions.
536 Cell Cycle. 2012;11(15):2808-18.
537 15. Laplantine E, Fontan E, Chiaravalli J, Lopez T, Lakisic G, Veron M, et al. NEMO specifically
538 recognizes K63-linked poly-ubiquitin chains through a new bipartite ubiquitin-binding domain. EMBO J.
539 2009;28(19):2885-95.
540 16. Mukherjea M, Llinas P, Kim H, Travaglia M, Safer D, Menetrey J, et al. Myosin VI dimerization
541 triggers an unfolding of a three-helix bundle in order to extend its reach. Mol Cell. 2009;35(3):305-15.
542 17. Yu C, Feng W, Wei Z, Miyanoiri Y, Wen W, Zhao Y, et al. Myosin VI undergoes cargo-mediated
543 dimerization. Cell. 2009;138(3):537-48.
544 18. Noguchi T, Frank DJ, Isaji M, Miller KG. Coiled-coil-mediated dimerization is not required for
545 myosin VI to stabilize actin during spermatid individualization in Drosophila melanogaster. Mol Biol Cell.
546 2009;20(1):358-67.
547 19. Sahlender DA, Roberts RC, Arden SD, Spudich G, Taylor MJ, Luzio JP, et al. Optineurin links
548 myosin VI to the Golgi complex and is involved in Golgi organization and exocytosis. J Cell Biol.
549 2005;169(2):285-95.
550 20. He F, Wollscheid HP, Nowicka U, Biancospino M, Valentini E, Ehlinger A, et al. Myosin VI
551 Contains a Compact Structural Motif that Binds to Ubiquitin Chains. Cell Rep. 2016;14(11):2683-94.

552 21. Wollscheid HP, Biancospino M, He F, Magistrati E, Molteni E, Lupia M, et al. Diverse functions of
553 myosin VI elucidated by an isoform-specific alpha-helix domain. Nat Struct Mol Biol. 2016;23(4):300-8.
554 22. Buss F, Kendrick-Jones J. How are the cellular functions of myosin VI regulated within the cell?
555 Biochem Biophys Res Commun. 2008;369(1):165-75.
556 23. Spudich G, Chibalina MV, Au JS, Arden SD, Buss F, Kendrick-Jones J. Myosin VI targeting to
557 clathrin-coated structures and dimerization is mediated by binding to Disabled-2 and PtdIns(4,5)P2. Nat
558 Cell Biol. 2007;9(2):176-83.
559 24. Batters C, Brack D, Ellrich H, Averbeck B, Veigel C. Calcium can mobilize and activate myosin-VI.
560 Proc Natl Acad Sci U S A. 2016;113(9):E1162-9.
561 25. Toettcher JE, Gong D, Lim WA, Weiner OD. Light-based feedback for controlling intracellular
562 signaling dynamics. Nat Methods. 2011;8(10):837-9.
563 26. Levskaya A, Weiner OD, Lim WA, Voigt CA. Spatiotemporal control of cell signalling using a light-
564 switchable protein interaction. Nature. 2009;461(7266):997-1001.
565 27. Bugaj LJ, Choksi AT, Mesuda CK, Kane RS, Schaffer DV. Optogenetic protein clustering and
566 signaling activation in mammalian cells. Nat Methods. 2013;10(3):249-52.
567 28. Kumar A, Ali AM, Woolley GA. Photo-control of DNA binding by an engrailed homeodomain-
568 photoactive yellow protein hybrid. Photochem Photobiol Sci. 2015;14(9):1729-36.
569 29. Strickland D, Yao X, Gawlak G, Rosen MK, Gardner KH, Sosnick TR. Rationally improving LOV
570 domain-based photoswitches. Nat Methods. 2010;7(8):623-6.
571 30. Strickland D, Lin Y, Wagner E, Hope CM, Zayner J, Antoniou C, et al. TULIPs: tunable, light-
572 controlled interacting protein tags for cell biology. Nat Methods. 2012;9(4):379-84.
573 31. Wu YI, Frey D, Lungu OI, Jaehrig A, Schlichting I, Kuhlman B, et al. A genetically encoded
574 photoactivatable Rac controls the motility of living cells. Nature. 2009;461(7260):104-8.

575 32. Christie JM, Salomon M, Nozue K, Wada M, Briggs WR. LOV (light, oxygen, or voltage) domains
576 of the blue-light photoreceptor phototropin (nph1): binding sites for the chromophore flavin
577 mononucleotide. Proc Natl Acad Sci U S A. 1999;96(15):8779-83.
578 33. Crosson S, Moffat K. Structure of a flavin-binding plant photoreceptor domain: insights into
579 light-mediated signal transduction. Proc Natl Acad Sci U S A. 2001;98(6):2995-3000.
580 34. Salomon M, Eisenreich W, Durr H, Schleicher E, Knieb E, Massey V, et al. An optomechanical
581 transducer in the blue light receptor phototropin from Avena sativa. Proc Natl Acad Sci U S A.
582 2001;98(22):12357-61.
583 35. Harper SM, Neil LC, Gardner KH. Structural basis of a phototropin light switch. Science.
584 2003;301(5639):1541-4.
585 36. Zayner JP, Antoniou C, Sosnick TR. The amino-terminal helix modulates light-activated
586 conformational changes in AsLOV2. J Mol Biol. 2012;419(1-2):61-74.
587 37. Zayner JP, Antoniou C, French AR, Hause RJ, Jr., Sosnick TR. Investigating models of protein
588 function and allostery with a widespread mutational analysis of a light-activated protein. Biophys J.
589 2013;105(4):1027-36.
590 38. Strickland D, Moffat K, Sosnick TR. Light-activated DNA binding in a designed allosteric protein.
591 Proc Natl Acad Sci U S A. 2008;105(31):10709-14.
592 39. Pudasaini A, El-Arab KK, Zoltowski BD. LOV-based optogenetic devices: light-driven modules to
593 impart photoregulated control of cellular signaling. Front Mol Biosci. 2015;2:18.
594 40. Yumerefendi H, Lerner AM, Zimmerman SP, Hahn K, Bear JE, Strahl BD, et al. Light-induced
595 nuclear export reveals rapid dynamics of epigenetic modifications. Nat Chem Biol. 2016;12(6):399-401.
596 41. Harper SM, Christie JM, Gardner KH. Disruption of the LOV-Jalpha helix interaction activates
597 phototropin kinase activity. Biochemistry. 2004;43(51):16184-92.

598 42. Guntas G, Hallett RA, Zimmerman SP, Williams T, Yumerefendi H, Bear JE, et al. Engineering an
599 improved light-induced dimer (iLID) for controlling the localization and activity of signaling proteins. Proc
600 Natl Acad Sci U S A. 2015;112(1):112-7.
601 43. Lacroix E, Viguera AR, Serrano L. Elucidating the folding problem of alpha-helices: local motifs,
602 long-range electrostatics, ionic-strength dependence and prediction of NMR parameters. J Mol Biol.
603 1998;284(1):173-91.
604 44. Kulic IM, Brown AE, Kim H, Kural C, Blehm B, Selvin PR, et al. The role of microtubule movement
605 in bidirectional organelle transport. Proc Natl Acad Sci U S A. 2008;105(29):10011-6.
606 45. Kapitein LC, van Bergeijk P, Lipka J, Keijzer N, Wulf PS, Katrukha EA, et al. Myosin-V opposes
607 microtubule-based cargo transport and drives directional motility on cortical actin. Curr Biol.
608 2013;23(9):828-34.
609 46. Kammerer S, Holzinger A, Welsch U, Roscher AA. Cloning and characterization of the gene
610 encoding the human peroxisomal assembly protein Pex3p. FEBS Lett. 1998;429(1):53-60.
611 47. Altman D, Sweeney HL, Spudich JA. The mechanism of myosin VI translocation and its load-
612 induced anchoring. Cell. 2004;116(5):737-49.
613 48. Morris CA, Wells AL, Yang Z, Chen LQ, Baldacchino CV, Sweeney HL. Calcium functionally
614 uncouples the heads of myosin VI. J Biol Chem. 2003;278(26):23324-30.
615 49. Furch M, Geeves MA, Manstein DJ. Modulation of actin affinity and actomyosin adenosine
616 triphosphatase by charge changes in the myosin motor domain. Biochemistry. 1998;37(18):6317-26.
617 50. Llinas P, Pylypenko O, Isabet T, Mukherjea M, Sweeney HL, Houdusse AM. How myosin motors
618 power cellular functions: an exciting journey from structure to function: based on a lecture delivered at
619 the 34th FEBS Congress in Prague, Czech Republic, July 2009. FEBS J. 2012;279(4):551-62.
620 51. Tumbarello DA, Kendrick-Jones J, Buss F. Myosin VI and its cargo adaptors - linking endocytosis
621 and autophagy. J Cell Sci. 2013;126(Pt 12):2561-70.

622 52. van Bergeijk P, Adrian M, Hoogenraad CC, Kapitein LC. Optogenetic control of organelle
623 transport and positioning. Nature. 2015;518(7537):111-4.
624 53. Duan L, Che D, Zhang K, Ong Q, Guo S, Cui B. Optogenetic control of molecular motors and
625 organelle distributions in cells. Chem Biol. 2015;22(5):671-82.
626 54. Aschenbrenner L, Naccache SN, Hasson T. Uncoated endocytic vesicles require the
627 unconventional myosin, Myo6, for rapid transport through actin barriers. Mol Biol Cell. 2004;15(5):2253-
628 63.
629 55. Le Roy C, Wrana JL. Clathrin- and non-clathrin-mediated endocytic regulation of cell signalling.
630 Nat Rev Mol Cell Biol. 2005;6(2):112-26.
631 56. Wuytack F, Raeymaekers L, Missiaen L. PMR1/SPCA Ca2+ pumps and the role of the Golgi
632 apparatus as a Ca2+ store. Pflugers Arch. 2003;446(2):148-53.
633 57. Li LH, Tian XR, Jiang Z, Zeng LW, He WF, Hu ZP. The Golgi Apparatus: Panel Point of Cytosolic
634 Ca(2+) Regulation. Neurosignals. 2013;21(3-4):272-84.
635 58. Papanikou E, Day KJ, Austin J, Glick BS. COPI selectively drives maturation of the early Golgi.
636 Elife. 2015;4.
637 59. Zhang Y, Werling U, Edelmann W. Seamless Ligation Cloning Extract (SLiCE) cloning method.
638 Methods Mol Biol. 2014;1116:235-44.
639 60. Townsley FM, Wilson DW, Pelham HR. Mutational analysis of the human KDEL receptor: distinct
640 structural requirements for Golgi retention, ligand binding and retrograde transport. EMBO J.
641 1993;12(7):2821-9.
642 61. Scheel AA, Pelham HR. Identification of amino acids in the binding pocket of the human KDEL
643 receptor. J Biol Chem. 1998;273(4):2467-72.

644 62. Kapitein LC, Schlager MA, van der Zwan WA, Wulf PS, Keijzer N, Hoogenraad CC. Probing
645 intracellular motor protein activity using an inducible cargo trafficking assay. Biophys J. 2010;99(7):2143-
646 52.
647 63. Rock RS, Rief M, Mehta AD, Spudich JA. In vitro assays of processive myosin motors. Methods.
648 2000;22(4):373-81.
649 64. Meijering E, Dzyubachyk O, Smal I. Methods for cell and particle tracking. Methods Enzymol.
650 2012;504:183-200.
651 65. Schneider CA, Rasband WS, Eliceiri KW. NIH Image to ImageJ: 25 years of image analysis. Nat
652 Methods. 2012;9(7):671-5.
653